Memoirs of the Faculty of Science, Kyoto University, Series of Physics, Astrophysics, Geophysics and Chemistry, Vol.XXXXII, No.1, Article 2, 2001

Upper Mantle P-wave Structure of the Northwestern Rim of the Pacific Ocean

By

Tadashi Sugiyama* and Ichiro Nakanishi†

(*Received October 31, 1997*)

Abstract

We analyzed the first and secondary waves recorded by the seismic network of the Research Center for Earthquake Prediction of Hokkaido University to obtain the upper mantle P-wave structure of the northwestern rim of the Pacific Ocean. We made a data set of 67 earthquakes which occurred at depths shallower than 100 km along the Kuril - Aleutian Arc ($6° < \Delta < 55°$) from April, 1985, to December, 1986. We read the first and secondary arrival times and determined the slowness and azimuth at the center of the network. The travel times of the first arrivals are approximately identical with the J-B times in the distance range except for $14° - 20°$, where they are earlier than the J-B times. The secondary waves are seen as back-branches in the travel time curve and positive gradients in the slowness curve in the distance ranges of $14° - 22°$ and $19° - 25°$. We obtained the one-dimensional P-wave structure which could explain the observations of both the travel time and slowness very well. No low velocity zone exists in the uppermost mantle, where the velocity increases with depth in the depth ranges of 33 - 95 km and 165 - 200 km and is constant in between. There are two transition zones where the velocity increases rapidly at depths of 400 km and 700 km and a minor transition zone at 460 km. The prominent difference between this model and the models obtained by the previous studies, for example Fukao (1977), is that it has no low velocity zone and the depth of the 660

*Shimizu-Minami High School, Shimizu 424-8622, Japan
†Department of Geophysics, Kyoto University, Kyoto 606-8502, Japan

km discontinuity is deep. Using a linear least-squares method with linear inequality constraints we made the $\tau - p$ inversion of the travel time data to obtain the best velocity model and the error bounds that include all velocity-depth curves which agree with the data within a statistical limit. The error bounds of the discontinuity at the depth of 700 km for a 95 % confidence level of our model includes the 660 km discontinuity of Fukao's model. It might be a little difficult to suggest the regional difference in the depth of the 660 km discontinuity on the basis of rigid statistical consideration. However, our recent study on the P-wave structure using a different seismic network (Kato and Nakanishi, 2000) supports the depth of 700 km obtained here for the discontinuity.

1 Introduction

It is well known that the seismic velocity increases discontinuously at depths of about 410 and 660 km in the upper mantle (Anderson and Toksöz, 1963; Niazi and Anderson, 1965; Johnson, 1967; Walck, 1984).

Advances in high-pressure experiments have reached a depth of about 800 km in the Earth's mantle (Ito and Takahashi, 1989). The upper mantle discontinuities are interpreted in terms of mineralogical phase relation in $Mg_2SiO_4 - Fe_2SiO_4$ system. High-pressure experiments of olivine (α) to modified spinel (β) transformation, which is considered to correspond to the 410 km discontinuity, suggest the transformation width of 11 to 19 km in temperature range of 1400 to 1750°C (Katsura and Ito, 1989). Ito and Takahashi (1989) show that the transformation of spinel (γ) to perovskite + magnesiowüstite takes place at pressure of 23.1 GPa with a pressure interval less than 0.15GPa at temperature of 1600°C. These pressure values are converted to depth of 653 km and a depth interval less than 5 km.

The reflected and converted waves from these upper mantle discontinuities have been observed clearly and fine structures of the discontinuities have been studied in both global and regional scales. Examples of those discontinuity-sensitive waves are precursors to P'P' (PKPPKP) (Engdahl and Flinn, 1969; Adams, 1971; Nakanishi, 1986, 1988, 1989), P-to-SV conversions (Vinnik, 1977; Kosarev et al., 1999), and precursors to SS (Shearer, 1991, 1993, 1996).

The information on the regional variations of the depth and structure of the discontinuities is indispensable for the discussion on dynamics in the earth mantle.

A drawback of the approaches using the reflected or converted waves is the difficulty in obtaining the absolute value of P or S wave velocity.

Analysis of refracted waves can overcome this difficulty at the expense of lateral resolution for velocity structure.

Several anothors have determined the P-velocity models of the upper mantle of the Japanese region by almost indentical methods (Kanamori, 1967; Fukao, 1977; Inatani and Kurita, 1980). Those models have different depths and velocity contrasts of the discontinuities. This difference is not only due to real mantle structure, but also due to non-uniqueness of the interpretation of data. We must collect many accurate data to know actual regional difference in the upper mantle structure.

In this study we attempt a P-wave analysis by using data from the seismic network of the Research Center for Earthquake Prediction of Hokkaido University (RCEP), Hokkaido, Japan, for the purpose of obtaining the upper mantle velocity structure beneath an area extending from the Kuril-Kamchatka Arc to the Aleutian Arc. Section 2 of this paper shows the data that we analyze. In section 3 we make an array analysis of refracted waves. In section 4 we construct P-wave velocity model. Regional difference found in this study is discussed with reference to the depression in 660 km discontinuity beneath the subduction region in section 5. Section 6 summarizes the results of this study.

2 Data

We use seismic waves recorded by the 18 stations network of RCEP. Figure 1 shows the station configuration of the network.

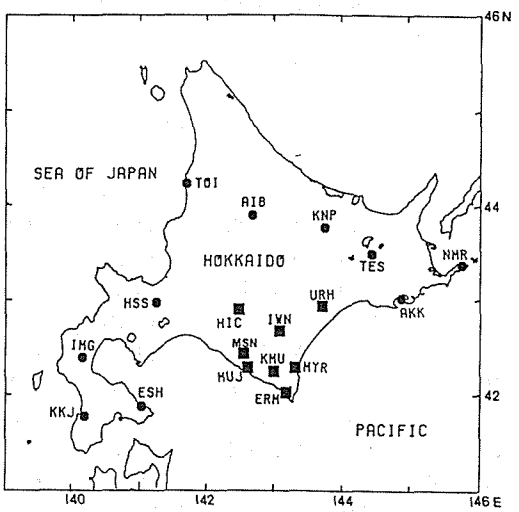

Figure 1: Map showing the locations of the 18 RCEP stations which we use in this paper.

First we searched the earthquakes which occurred in the region extending from the Kuril Islands to southern Alaska in April - December of 1985 by referring to the PDE (Preliminary Determination of Epicenters) monthly list. Then we picked up only the earthquakes which were successfully recorded at RCEP stations and located at depths shallower than 100 km. The reason why we restricted the analysis to only relatively shallow events was to keep the error due to depth correction as small as possible. The number of the events thus selected was 55.

We found the absence of events in the distance range of about $23° - 37°$. Thus we searched events in that epicentral range in the data of January - December, 1986, and found 7 events. We took 5 events from the data set of Nakanishi and Motoya (1990). The events used in this study totaled 67.

Table 1 shows the source parameters, epicentral distances and azimuths calculated for station HIC (Hidaka), the center of the network, after the source depth correction. Here the parameters are not taken from the PDE list but from the bulletin of ISC (International Seismological Centre) because we consider that the latter is more reliable than the former. In fact, the comparison of the travel times based on the two kinds of parameters shows a little disagreement.

Table 1. Earthquake List

ev	date			origin time			epicenter		dep	m_b	dist	azim
no	y	m	d	h	m	s	deg	deg	km		deg	deg
1	1985	4	12	0	0	43.0	N43.89	E148.60	45	4.6	7.11	75.34
2	1985	4	12	10	16	4.7	N56.31	E162.34	33	4.8	18.96	36.64
3	1985	4	12	21	53	58.5	N45.25	E150.42	70	4.5	8.83	64.94
4	1985	4	14	21	39	4.0	N47.33	E153.04	33	4.7	8.90	55.70
5	1985	4	18	0	6	30.9	N52.16	E159.57	18	5.6	15.15	45.26
6	1985	4	18	4	6	49.5	N52.15	E159.64	39	4.9	15.07	45.38
7	1985	4	25	3	10	7.5	N46.52	E154.10	37	5.1	9.34	62.38
8	1985	4	25	13	49	2.7	N56.23	E164.20	39	4.9	19.78	38.74
9	1985	5	2	8	55	16.0	N48.83	E156.19	42	5.9	11.76	53.45
10	1985	5	2	12	52	28.0	N56.17	E163.30	24	5.1	19.15	38.00
11	1985	5	10	3	51	38.1	N47.70	E152.40	52	4.6	9.35	52.13
12	1985	5	12	7	13	26.7	N52.12	E159.15	70	4.7	15.35	44.85
13	1985	5	16	10	22	50.4	N48.37	E155.53	54	5.1	11.45	54.60
14	1985	5	19	8	7	47.0	N53.57	E160.53	54	6.0	16.46	42.02
15	1985	6	3	23	53	44.1	N44.02	E147.86	71	4.8	8.70	72.16
16	1985	7	15	5	32	56.0	N53.81	E161.47	29	4.7	16.86	42.41
17	1985	7	17	12	13	22.0	N52.04	E160.01	8	5.1	15.25	46.21

Table 1. Earthquake List (continued 1)

ev	date			origin time			epicenter		dep	m_b	dist	azim
no	y	m	d	h	m	s	deg	deg	km		deg	deg
18	1985	7	25	18	59	57.0	N45.17	E150.11	50	5.0	7.54	64.96
19	1985	7	29	6	32	18.5	N56.10	E164.54	37	5.2	19.82	39.39
20	1985	7	29	18	31	38.3	N49.50	E156.20	63	4.6	12.62	50.48
21	1985	7	30	5	35	37.4	N44.90	E149.30	33	4.4	6.60	65.57
22	1985	7	31	7	37	52.0	N52.40	E173.44	25	5.7	23.09	54.55
23	1985	8	5	20	23	37.4	N53.59	E160.40	33	5.0	16.23	41.80
24	1985	8	9	13	3	10.6	N52.44	E173.56	35	5.5	23.13	54.49
25	1985	8	9	22	24	9.3	N56.16	E162.75	45	5.1	19.26	37.46
26	1985	8	9	23	7	2.7	N56.30	E162.60	33	4.7	19.08	36.95
27	1985	8	11	9	59	42.0	N54.15	E168.69	29	5.9	20.39	47.72
28	1985	8	13	12	50	39.0	N43.80	E150.10	33	4.7	6.66	78.15
29	1985	8	24	9	9	1.1	N43.45	E147.07	54	4.6	7.60	79.04
30	1985	8	26	2	26	40.0	N45.40	E148.40	33	4.5	6.57	57.58
31	1985	8	31	12	31	50.2	N55.40	E163.70	33	4.9	19.06	40.38
32	1985	9	1	14	7	30.3	N49.30	E155.80	33	4.5	11.55	50.71
33	1985	9	1	21	58	2.6	N43.77	E148.03	68	4.8	8.50	75.92
34	1985	9	9	15	17	59.6	N46.28	E153.29	10	5.4	8.39	62.63
35	1985	9	18	1	27	15.7	N49.59	E155.74	41	5.6	11.86	49.33
36	1985	9	18	23	53	19.9	N47.78	E154.06	45	4.8	10.03	55.12
37	1985	9	27	2	6	29.2	N46.85	E153.53	34	4.9	9.03	59.49
38	1985	10	2	3	16	26.0	N43.73	E151.25	40	5.4	7.30	79.57
39	1985	10	9	9	33	32.6	N54.73	W159.65	30	6.1	39.16	51.59
40	1985	10	16	15	23	42.5	N48.10	E154.10	33	4.5	9.89	53.49
41	1985	10	24	19	10	25.0	N44.35	E148.60	70	4.5	8.64	69.81
42	1985	10	26	15	59	36.9	N54.82	W159.57	40	5.5	39.42	51.44
43	1985	10	28	14	54	40.0	N54.70	E162.10	33	4.8	17.76	40.59
44	1985	11	14	22	17	46.2	N55.02	W160.12	33	5.4	39.01	51.18
45	1985	11	15	11	56	18.0	N43.95	E148.42	40	5.1	6.86	74.28
46	1985	11	15	15	40	29.8	N49.60	E155.80	33	4.8	11.71	49.39
47	1985	11	15	18	42	46.5	N47.40	E153.10	33	4.5	8.97	55.41
48	1985	11	17	7	30	29.0	N53.77	E160.43	44	5.1	16.42	41.30
49	1985	11	20	5	14	27.1	N43.66	E148.48	40	5.0	6.86	78.05
50	1985	12	1	4	48	5.3	N43.69	E148.94	38	4.9	6.77	78.22
51	1985	12	6	8	55	34.6	N44.66	E148.70	95	4.7	10.28	66.51
52	1985	12	6	12	33	22.2	N49.63	E157.15	42	5.0	12.73	51.37
53	1985	12	19	5	16	2.8	N52.86	E159.60	0	5.1	15.20	43.03
54	1985	12	23	0	1	23.6	N46.54	E152.61	51	5.2	8.98	59.75
55	1985	12	28	7	44	36.0	N56.56	W156.59	39	5.2	40.19	48.40

Table 1. Earthquake List (continued 2)

ev	date			origin time			epicenter		dep	m_b	dist	azim
no	y	m	d	h	m	s	deg	deg	km		deg	deg
56	1986	3	2	20	42	28.8	N51.60	W176.78	55	5.1	29.71	58.04
57	1986	5	8	1	11	2.3	N51.09	W176.70	32	5.8	29.31	59.11
58	1986	5	8	5	37	20.4	N51.34	W175.41	18	5.9	29.60	58.58
59	1986	5	17	16	20	23.7	N52.26	W174.29	26	5.7	30.37	56.75
60	1986	6	18	8	5	15.7	N51.66	W176.90	56	5.8	29.64	57.91
61	1986	7	19	4	31	57.7	N53.38	W165.91	46	5.5	35.25	54.40
62	1986	11	6	18	27	1.1	N51.43	W176.68	40	5.2	29.56	58.40
63	1985	5	24	22	4	44.5	N51.41	W178.43	43	5.7	28.18	58.37
64	1985	10	5	15	24	2.5	N62.22	W124.26	10	6.4	54.58	35.03
65	1986	1	18	1	58	59.0	N51.54	W173.11	13	5.8	30.94	58.16
66	1986	6	19	9	9	10.1	N56.39	W152.86	17	5.9	42.36	48.20
67	1986	9	12	23	57	15.8	N56.19	W153.40	31	6.0	41.67	48.53

Figure 2 shows the locations of the 67 events. They occurred along the Kuril-Kamchatka Arc and the Aleutian Arc. The range of the azimuth of the events extends about 60°. The epicentral distribution bends abruptly at the junction of the two arcs. This causes a large change in the epicenter azimuth.

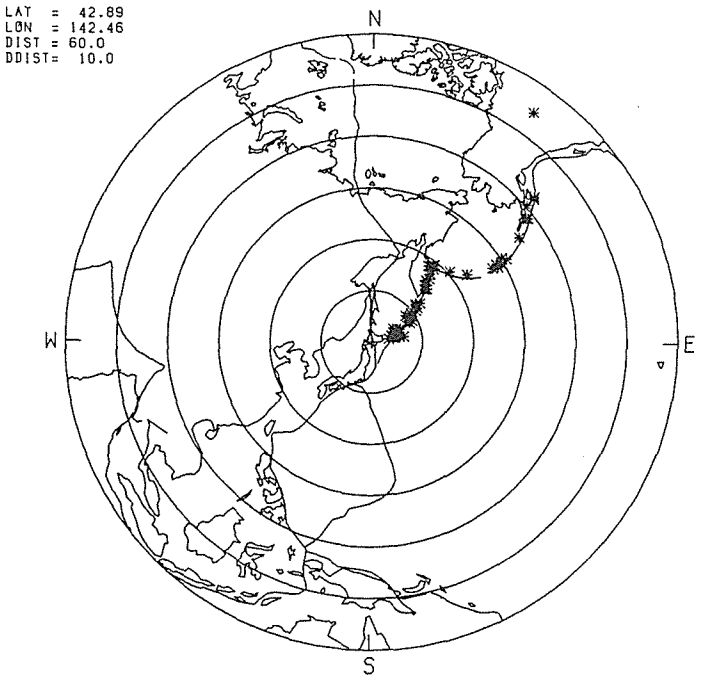

Figure 2: Epicenters of the 67 earthquakes used in this study. Equidistant azimuthal projection is used. The center of circles is the array center. The circles are drawn at an interval of ten degrees.

3 Interpretation of data

3.1 Seismograms

Figure 3 shows the seismograms that are lined up according to the epicentral distance to find the correlation of the first and secondary phases among the stations. The seismograms are high-cut filtered at a frequency of 3.0 Hz to make the correlation apparent. The amplitude is normalized to the maximum of each trace. In the figure letter JB represents the arrival time of J-B tables (Jeffreys and Bullen, 1940). We summarize the characteristics of the first and secondary phases in four epicentral distance ranges.

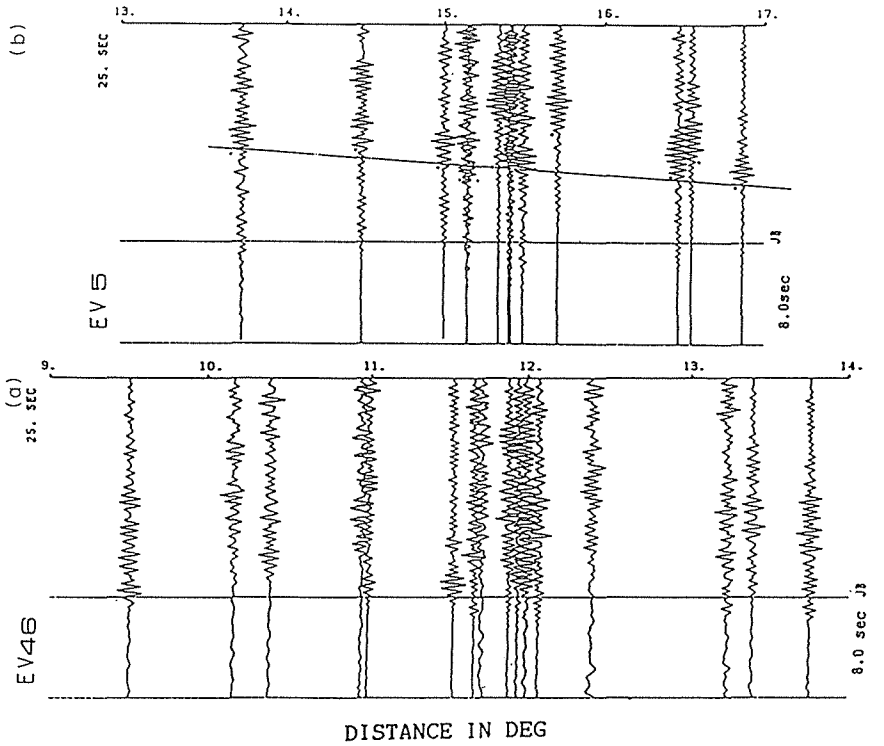

Figure 3 (a), (b): The seismograms high-cut filterd at a frequency of 3.0 Hz. The traces are lined up in order of the epicentral distances. They start 8.0 s before the J-B times. (a) event 46, (b) event 5.

$\Delta = 9° - 14°$ (Fig. 3(a), event 46 in Table 1). The first arrival times at distances nearer than 11° are almost identical with JB but are earlier than JB at distances beyond 11°. We can identify no secondary phase in this figure.

$\Delta = 14° - 17°$ (Flg. 3(b), event 5 in Table 1). The travel times of the first arrivals are earlier than JB and their amplitudes are small. We can

identify remarkable secondary phases with large amplitudes which correlate well between all traces. The travel time difference of the first and secondary waves decreases with distance. The slowness of this remarkable phase is determined to be 11.72 sec/deg by the method as described in a later section. We consider that this is a refracted wave from the 410 km discontinuity, which is called BC branch in this paper (see Fig. 12(a)).

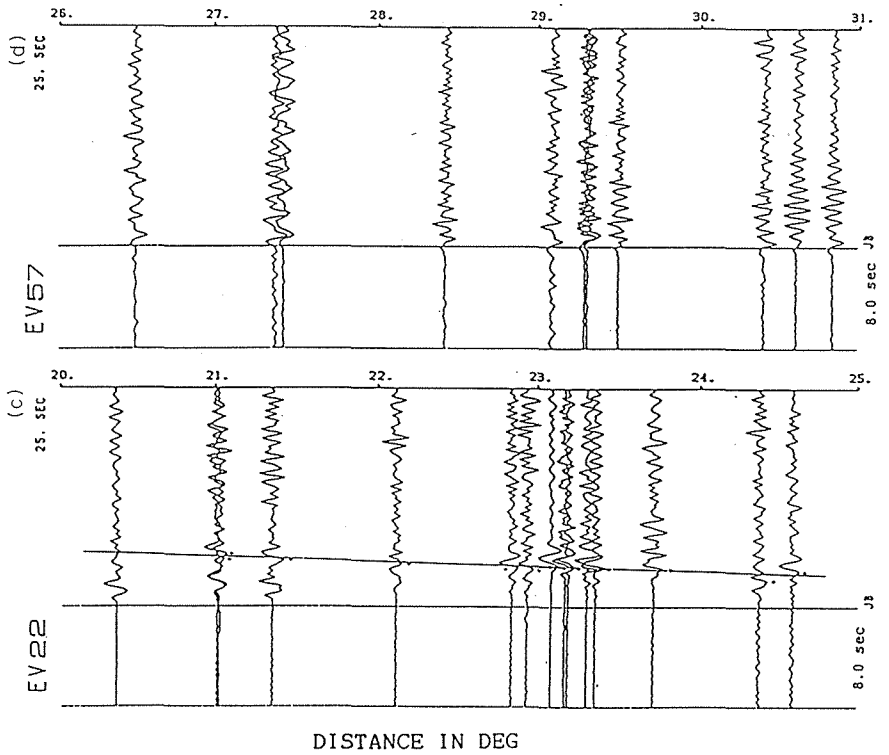

Figure 3 (c), (d): The seismograms high-cut filterd at a frequency of 3.0 Hz. The traces are lined up in order of the epicentral distances. They start 8.0 s before the J-B times. (c) event 22, (d) event 57.

$\Delta = 20° - 25°$ (Fig. 3(c), event 22 in Table 1). The travel times of the first arrivals are identical with JB. The arrivals are very clear especially around 21°. This may suggest the existence of a transition zone at a deph of about 500 km. We can identify the secondary phase that arrives a few seconds late after the first arrivals in this figure. The travel time difference gradually decreases with distance. The slowness of this secondary phase is 9.20 sec/deg. We consider this to be the phase which is turned back from the 660 km discontinuity (DE branch, see Fig. 12(a)).

$\Delta = 26° - 31°$ (Flg. 3(d), event 57 in Table l). The first arrival times are identical with JB. There is no secondary phase well correlated through all the traces in this figure.

We use here the J-B arrival time after correcting the effects due to hypocenter depth, station elevation, the Earth's ellipticity (Dziewonski and Gilbert, 1976) and the anomalies of velocity structure beneath the network (Nakanishi and Motoya, 1990).

Figure 4 shows a record section of 74 seismograms which have relatively good S/N ratios so that we can recognize the triplications.

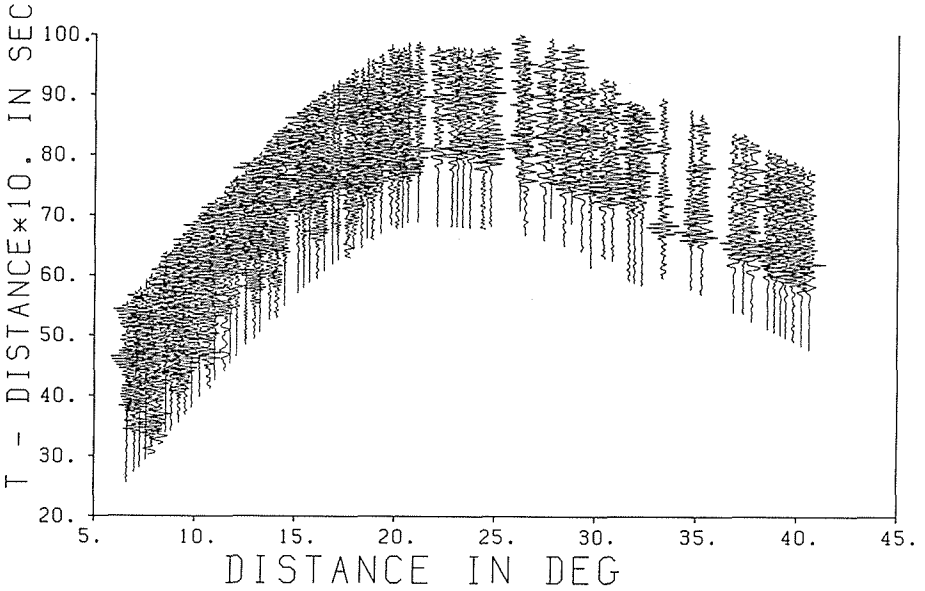

Figure 4: Data record section of 74 seismograms. They were obtained by resampling all the data at 0.25° distance interval in the range $6° - 40°$. The records are high-cut filtered at a frequency of 3.0 Hz. Each trace is normalized to its maximum amplitude.

3.2 Travel time

Figure 5(a) is a plot of the travel times of the selected events with clear arrivals. Fig. 5(b) shows the means and standard deviations of the travel times for the distance interval of 1°. It is likely that there are two groups of secondary arrivals which have nearly constant gradients in this plot. One extends over the distance range of $14° - 22°$ and the other $19° - 25°$. These may correspond to the backbranches of the 410 and 660 km discontinuities, respectively.

3.3 Slowness and azimuth

Assuming that an arrival is a plane wave, one can calculate the slowness and azimuth of the arrival. We use a method of Walck and Minster (1982)

for that purpose. We calculate the slowness and azimuth only for the events which produce records with good S/N ratios at more than eight stations.

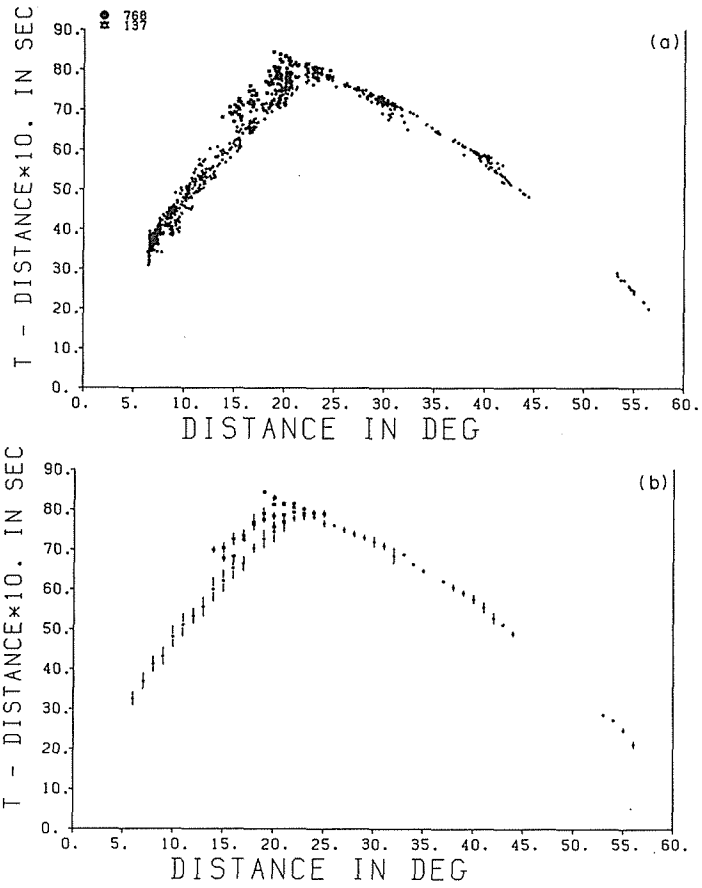

Figure 5: Reduced travel time data of 67 earthquakes. (a) 768 first arrivals (solid circles) and 137 secondary arrivals (open triangles) are plotted after the corrections of source depth, station elevation, the Earth's ellipticity and velocity anomalies right beneath the stations. (b) The means and standard deviations of the travel time data (a) obtained for a distance interval of 1° for each branch.

Figure 6 shows the slownesses and azimuths thus determined. We point out some remarkable features in this figure.

Slowness (Fig. 6 (a)): The slowness decreases with distance and its slope changes rapidly at a distance of about 25°. On the contrary, the slowness increases with distance in the distance ranges of 15° to 18° and 18° to 23°. These may be the BC and DE branches originating from the 410 and 660 km discontinuities. There is a gap at about 20° where the slowness abruptly drops and the values of the first and secondary waves are mixed

there. It appears that this corresponds to the sudden decrease in slowness that Fukao (1977) and Kanamori (1967) have already pointed out, though its apparent distance differs from their results. We take their interpretation that the observation requires the introduction of a minor velocity transition zone between the two major discontinuities at 410 and 660 km.

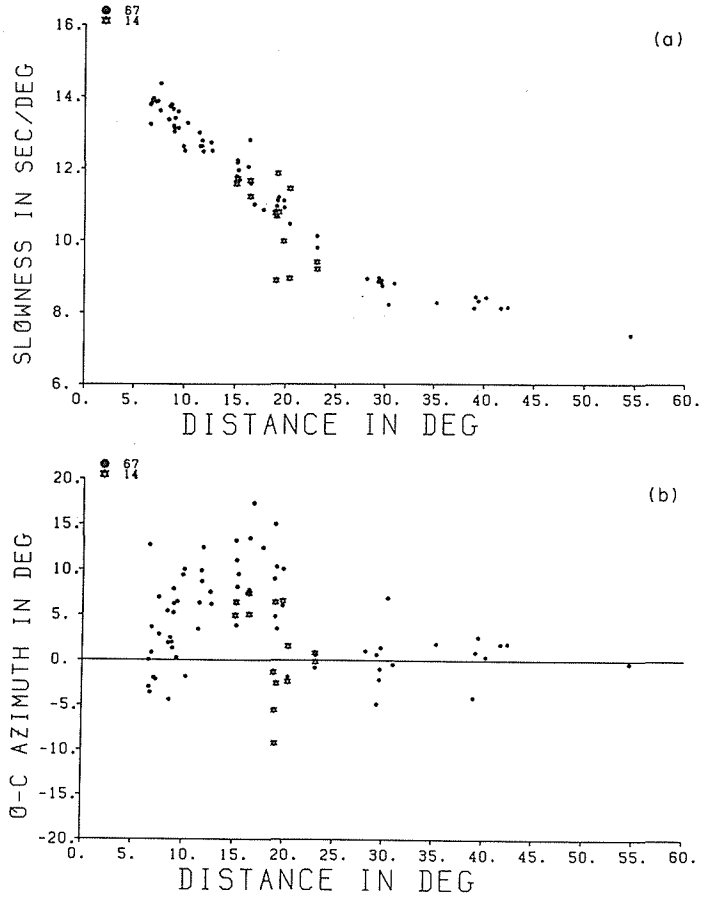

Figure 6: Results of the array analysis. (a) The slownesses of 67 first phases (solid circles) and 14 secondary phases (open triangles). (b) The difference between the azimuth obtained by the observed data and the one expected from the relation of the epicenter and the array center. The azimuth is measured clockwise from the north.

Azimuth (Fig. 6(b)): The result shows that the waves from events at distances shorter than 20° arrive at the network from the direction further south than the expected direction. On the contrary, at distances beyond 20° the waves arrive from the expected direction. This means that the wave propagates nearly within a vertical plane including the hypocenter and the network center. These characteristics in the observed azimuths are consistent

with the epicenter distribution of Fig. 2. One notices that the distance of 20° where the trend of the residual azimuth changes largely is the position of the junction of the Kuril-Kamchatka Arc and the Aleutian Arc (Fig. 2). According to Utsu (1971) the Pacific Plate descends under the Okhotsk Sea from the southeast to the northwest along the Kuril Arc. The seismic waves from the events located at distances greater than 20° leave the Pacific plate quickly and travel through the area of the oceanic side of the mantle. On the other hand, those with epicentral distances less than 20° initially leave the hypocenters approximately parallel to the strike of the discending Pacific plate and then arrive at the network after turning off into the oceanic side mantle because it is a few percents higher in P-velocity than the continental side mantle (Utsu, 1971; Hamada, 1973).

In the parameter determination by a least-squares method, the decrease of the number of parameters increases the precision of the solution. We also determined the slowness by fixing the azimuth to the value expected from the network and epicenter location. Figure 7 shows the result. If the residual azimuth seen in Fig. 6(b) were insignificant, the results in Figs. 6(a) and 7 must be identical and the result in Fig. 7 which did not suffer from the error due to the trade-off between the parameters would be more reliable. But in reality both are very different at distances less than 20° and the result in Fig. 7 is more scattered. This means the azimuth deviation in Fig. 6(b) is not negligible.

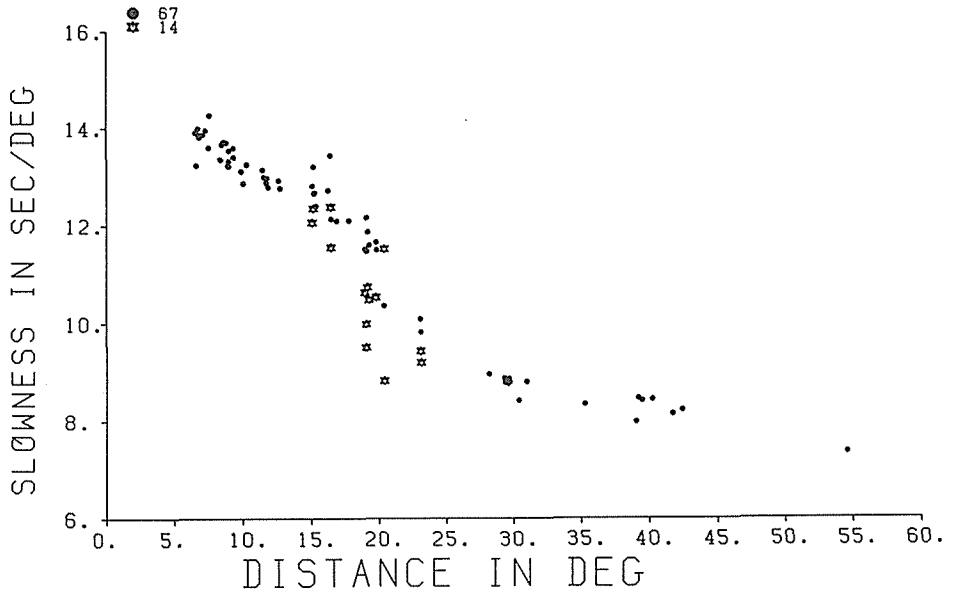

Figure 7: The slowness determined on the assumption that the azimuth is equal to the expected value.

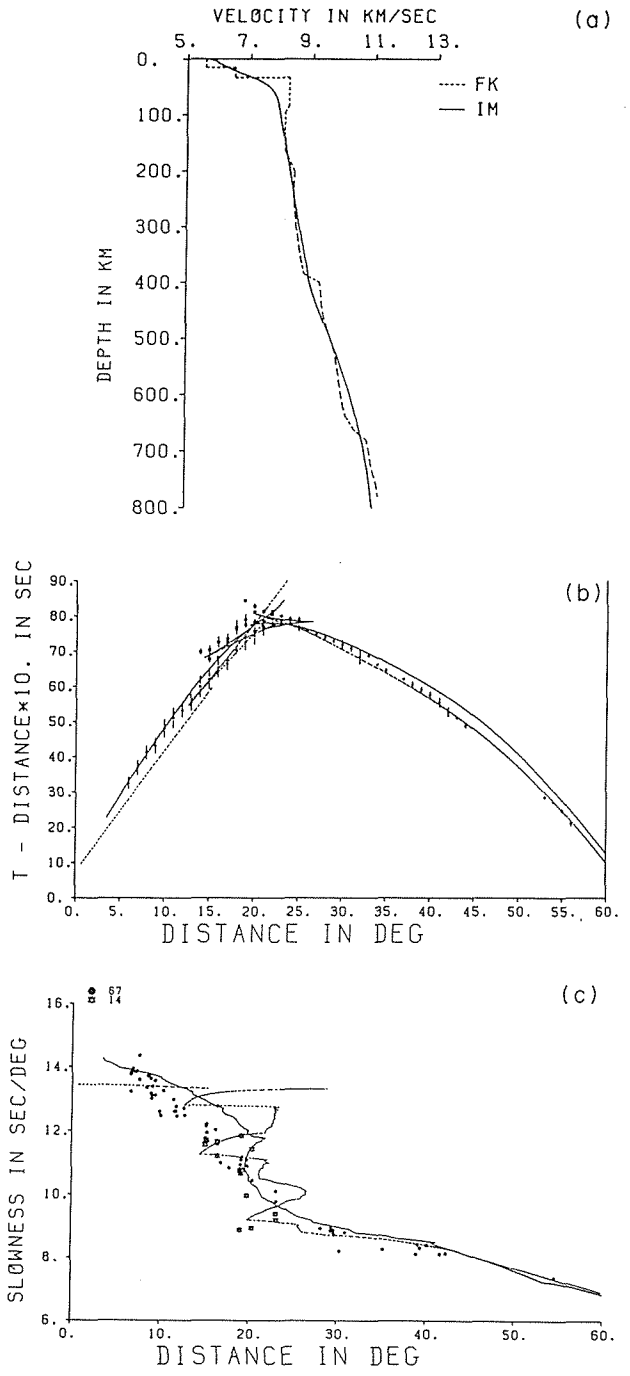

Figure 8: (a) Ichikawa and Mochizuki model (Ichikawa and Mochizuki, 1971; Hamada, 1984) is indicated by the solid line and Fukao (1977) model by the dashed line. (b) The comparison of the travel time curves calculated for the two models (solid and dashed lines) with the observations (Fig. 5(b)). (c) The comparison of the slowness curves with the observations (Fig. 6(a)).

4 Modeling

4.1 Shallow structure

For the modeling, it is necessary that the shallow structure is established. Unfortunately we can not obtain enough information about the shallow structure from the data described above. Therefore we must introduce some assumptions on the shallow structure in the modeling of the deep structure.

Fukao (1977) presented an upper mantle model of the ocean side of the Japan-Kuril Arc by analyzing the Kuril-Kamchatka events observed by an array in the Kii Peninsula, central Japan. The study area of this paper neighbors on that of Fukao, being just shifted to the north. On the other hand, Ichikawa and Mochizuki (1971) made a velocity model by using the explosion seismic data down to the depth of 35 km and the Jeffreys velocity model for greater depths. Their model was reexamined by Hamada (1984). This model may represent an average shallow structure of Japan.

Figure 8(a) shows the velocity-depth models of Fukao (1977) (FK) and Ichikawa and Mochizuki (1971)(IM), of which the travel times and slownesses are compared with the observations (Figs.5(b) and 6(a)) in Figs.8(b) and (c). Here we are concerned with the observations of the first arrivals at distances less than 20°.

The travel times of the first arrivals of FK are about 5 s earlier than the observations at distances less than 13° but are in agreement in the range $13° - 20°$. Though the first arrivals of FK in the range $13° - 15°$ are also too early, it is likely that we consider the secondary phase arriving a few seconds late as the first arrival in the same distance range because the amplitude of the latter is larger than that of the former. On the other hand, IM is in agreement with the observations at distances less than 13° but is too late in the range $13° - 20°$.

The slowness of FK takes nearly an average value of the observations at distances less than 10°. The slowness of IM is obviously too large in the same distance range.

As already mentioned, we determine the slowness on the assumption of a plane wave approximation. It is reasonable for teleseisms but the waves generally propagate as spherical waves in the case of near earthquakes which we deal with in this section. Therefore the obtained slownesses do not necessarily present real values. In the case of the travel time we are not afraid of the influence of the non-planar wave front. Considering these we decided to find the shallow model which mainly satisfies the travel time data.

Figure 9(a) shows three models which are obtained by changing the velocity at the depth of 33 km in model FK. The velocity values at that depth

are 8.00 km/s (model 1), 7.84 km/s (model 2), and 7.70 km/s (model 3). On the other hand, three models in Fig. 9(b) are those obtained by keeping a constant velocity in the depth range of 33 km to about 150 km. The constant velocity is 8.10 km/s (model 4), 8.00 km/s (model 5), and 7.84 km/s (model 6). Figures 10(a) and (b) compare the observed travel times with the calculated curve for each model. The travel times of model 1 and model 4 are too early at distances less than 12° and consistent beyond that distance. Model 2 is approximately consistent up to 20°, but is a little early at near distances. Model 3 is consistent at short distances and early at long distances in comparison with model 2. Model 5 is too early at near distances and somewhat late at far distances. Model 6 is consistent at distances less than 11° and too late beyond that distance.

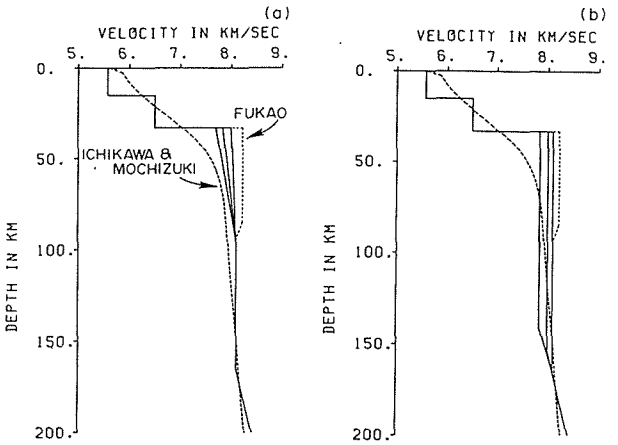

Figure 9: The trial models for the shallow structure. The dashed lines represent Ichikawa and Mochizuki model and Fukao model (Fig. 8(a)). (a) The velocity has a constant depth gradient at depths from 33 km to 95 km. The velocity at 33 km depth is 8.00 km/s (model 1), 7.84 km/s (model 2), and 7.70 km/s (model 3). (b) The velocity is constant at depths from 33 km to about 150 km. The velocity at 33 km depth is 8.10 km/s (model 4), 8.00 km/s (model 5), and 7.84 km/s (model 6).

From the comparison we can say the following. (1) Velocity at the depth of 33 km is lower than 7.84 km/s. (2) The mean velocity in the depth interval of 33-100 km is nearly equal to or a little smaller than 8.00 km/s. (3) It is easier to explain the observed travel times by the model whose velocity gradually increases with depth than the model with a constant velocity value.

Therefore if the velocity at 33 km depth is between 7.70-7.84 km/s like models 2 and 3 of Fig. 9(a), the agreement with the observations is acceptable. Finally we select model 2 for the shallow structure, considering the secondary arrivals at the end of AB branch.

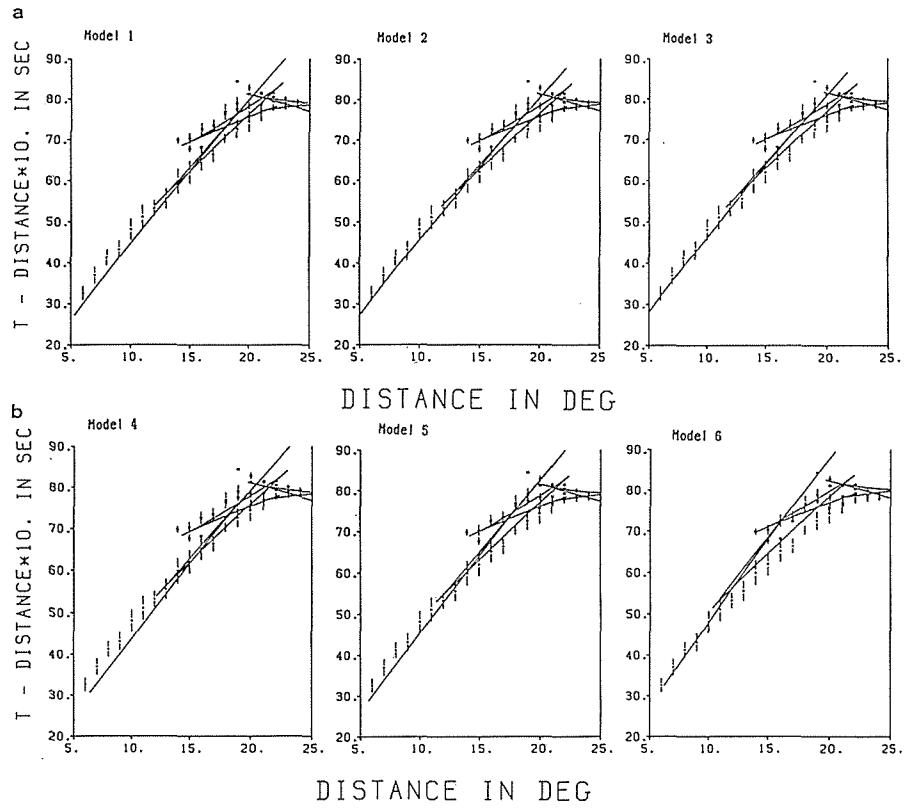

Figure 10: The comparison of the calculated travel times for models 1 to 6 with the observations.

4.2 Low velocity zone

One of the prominent features of the upper mantle structure that some have pointed out is the existence of a low velocity zone (LVZ) in the depth range of 70-200 km (Johnson, 1967; Kanamori, 1967). However, model 2 which we select above does not have it. The lid velocity of 8.23 km/s at 33 - 85 km depths and the LVZ velocity of 8.1 km/s at 95 - 165km of FK are rather high as compared with other models, such as Kanamori's (1967) model. As already mentioned the lid velocity of 8.23 km/s is too high to explain the travel time data of this study. If we allow the lid of a relatively low velocity, it is difficult to put further LVZ below the lid. Therefore it is difficult to find a model which has LVZ and satisfies the travel time data.

Furthermore the travel time curve for a model with LVZ must have a gap in the travel time, which becomes the very evidence for LVZ. It does not seem that there is such a gap in the observed travel time curve (Fig. 5). Thus we decide to use the model of the uppermost mantle without LVZ as shown in the above section (model 2).

Recently the existence of a strong LVZ has been questioned at least in the oldest part of the northwestern Pacific (Kawasaki et al., 1989). Several studies on the body wave travel times for the oceanic side of the Japan Arc have shown that LVZ is absent or that if it exists the velocity contrast is very small. Our analysis does not rule out a LVZ with such small velocity contrast.

4.3 Transition zone

Generally if the depth of a velocity discontinuity is increased, the travel times of the rays with turning points deeper than that depth become late and the triplication is formed at greater distances, which appears as the right shifted slowness on the slowness-distance diagram. If the velocity contrast is increased, the travel time becomes early, the end point C of the triplication goes back to a near distance, and it is indicated as greater slowness step on the slowness-distance diagram. Model 10 is obtained in such a way that the structure down to 400 km explains the observed travel times of the AB branch. The model is also consistent with both the travel time and slowness data of the BC back branch, which arrives as the secondary wave at distances from 22° to 14°. Because the branches are controlled by the depth and velocity contrast of the 400 km discontinuity, we use the 400 km discontinuity of model 10 in the modeling below.

We change the velocity profile at depths greater than 400 km of model 10. Figure 11 and Table 2 present model 12 thus obtained. We can explain the abrupt drop of the slowness at about 20° in the data by putting a transition zone of 3 % velocity contrast in the interval of 40 km around 460 km depth.

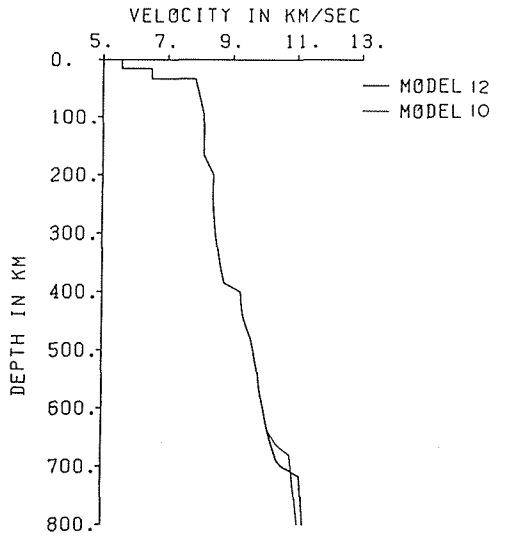

Figure 11: Models 12 and 10.

Table 2. Model 12 (Depth variation of P-velocity)

Dep	Vel	Dep	Vel	Dep	Vel	Dep	Vel
km	km/s	km	km/s	km	km/s	km	km/s
0	5.57	240	8.40	440	9.33	640	10.12
15	5.57	260	8.42	460	9.44	660	10.22
15	6.50	280	8.45	480	9.58	680	10.34
33	6.50	300	8.48	500	9.66	690	10.40
33	7.84	320	8.53	520	9.72	700	10.55
95	8.10	340	8.58	540	9.80	717	11.10
165	8.10	360	8.65	560	9.82	800	11.19
200	8.41	385	8.75	580	9.88		
205	8.41	400	9.25	600	9.96		
225	8.40	420	9.27	620	10.04		

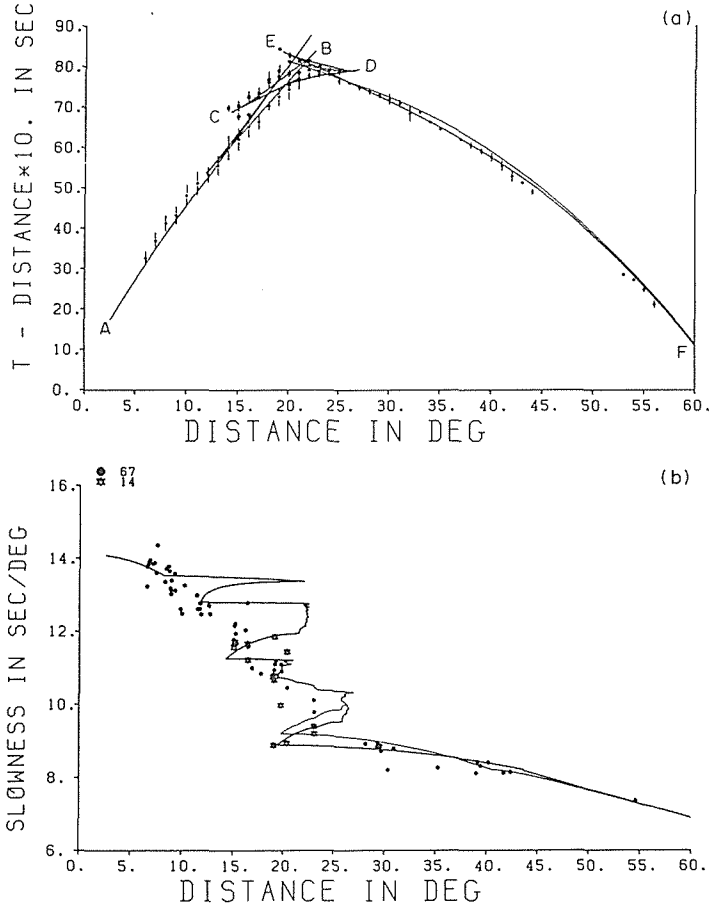

Figure 12: The comparison of the travel time and slowness for model 10 (normal line) and 12 (heavy line) with the observations. (a) Travel time. Letters refer to travel time branches discussed in text. (b) slowness.

Figure 12 compares the travel time and slowness of models 12 and 10 with the observations. The calculated travel time of CD branch, which is influenced by the velocity structure in the range from 400 km to the upper boundary of the second discontinuity, is consistent with the observations. Putting a discontinuity of 7 % contrast around 700 km depth (model 12) we can explain the DE branch which is inconsistent with model 10. The slowness is consistent at the end E of the DE branch.

It is apparent that model 12 that explains our data is similar to FK except for some differences. (1) The low velocity zone is absent. (2) The second discontinuity has a deeper depth of 700 km and a larger velocity contrast of 7 %. (3) The depth of the minor transition zone around 460 km is shallower by 40 km. This shallow start of the transion zone is also found in the model of Kanamori (1967). (4) The minor transition zone around 740 km is absent.

4.4 $\tau - p$ inversion and error bounds

We performed the inversion of the travel time data to velocity structure by the $\tau - p$ method of Stark and Parker (1987) (see also Stark et al. (1986) and Lawson and Hanson (1974)). τ means the time intercept of the travel time curve and is defined by the equation:

$$\tau(p) = T(X) - pX,$$

where p is the ray parameter, T the travel time, and X the epicentral distance.

We obtain the $\tau - p$ relation from the observed (X, T) data following Bessonova et al. (1974) (see also Aki and Richards, 1980). If the travel time curve were ideal, τ or X would be a single-valued function of p. However, the observed travel time of secondary wave is not necessarily a smooth convex or concave curve due to reading errors and lack of data, and τ or X might have two values for one ray parameter. We make single-valued $\tau - p$ and $X - p$ relations by selecting relatively well determined data.

Figure 13 shows the $\tau - p$ and $X - p$ relations thus obtained from the travel time data in Fig. 5(b). Because the observation at distances beyond 44° is sparse (Fig. 5(b)), we use only the data at distances less than 44°.

To obtain the error bounds that include all velocity-depth curves which agree with the observational $\tau(p)$ and $X(p)$ data within a statistical limit, we take the approach of Stark and Parker (1987) and adopt the following

function as the measure of misfit:

$$\mu(M) = \sum_{i=1}^{n_\tau}((\bar{d}_i - \tau_i(M))/\sigma_i)^2 + \sum_{i=n_\tau+1}^{n}((\bar{d}_i - X_i(M))/\sigma_i)^2,$$

where $\bar{d}_i$ and σ_i are the means and standard deviations of data, τ for $i = 1,\ldots,n_\tau$ and X for $i = n_\tau + 1,\ldots,n$. $\tau_i(M)$ and $X_i(M)$ are the τ and X calculated for model M. The depths for which the misfit function $\mu(M)$ is equal to the statistical limit suggested by the χ^2 distribution of a confidence level given *a priori* define the upper and lower error bounds of the depth for a target velocity. An iteration of finding the bounds for different target velocities results in the error bounds for an optimum velocity profile.

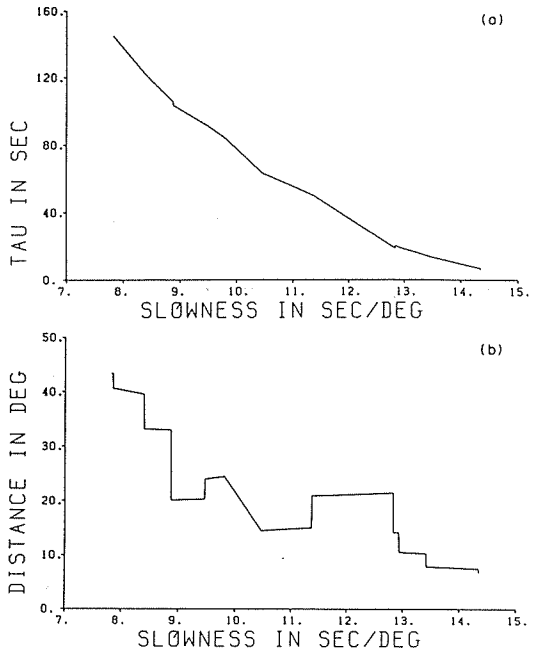

Figure 13: $\tau - p$ and $X - p$ relations obtained from the travel time curves of Fig. 5(b).

Figure 14 is the model (model 14) which is obtained by assuming the structure of model 2 at depths shallower than 191.6 km. The model has two major discontinuities at 460 and 720 km. As compared with model 12 the 400 km discontinuity of model 14 is deep and great in velocity contrast. Both models have similar depths and velocity contrasts of the 660 km discontinuity.

Figure 14 shows the error bounds obtained with the confidence level of 99.5 %. The width of the bounds is 40 km for the first discontinuity (445-485 km) and 70 km for the second discontinuity (685-752 km) of model 14. The depth of the 410 km discontinuity of model 12 is far shallower than the upper bound of the depth of the discontinuity.

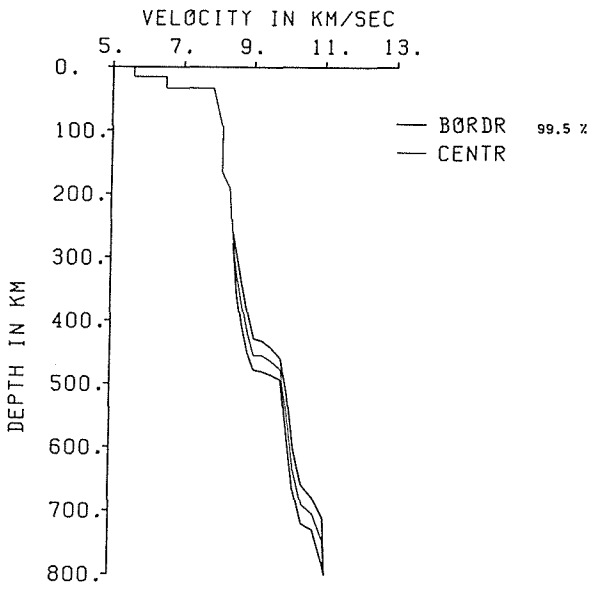

Figure 14: The best velocity model (CENTR) (model 14) and its error bounds (BORDR) obtained by the $\tau - p$ inversion. The confidence level is 99.5 %. The depth of the stripping is 191.6 km.

Figure 15 is the comparison of the calculated travel time for model 14 with the observations. The figure shows that model 14 can explain overall trend of the travel time but not the details of the triplications, such as the positions of C and E (Fig.12(a)).

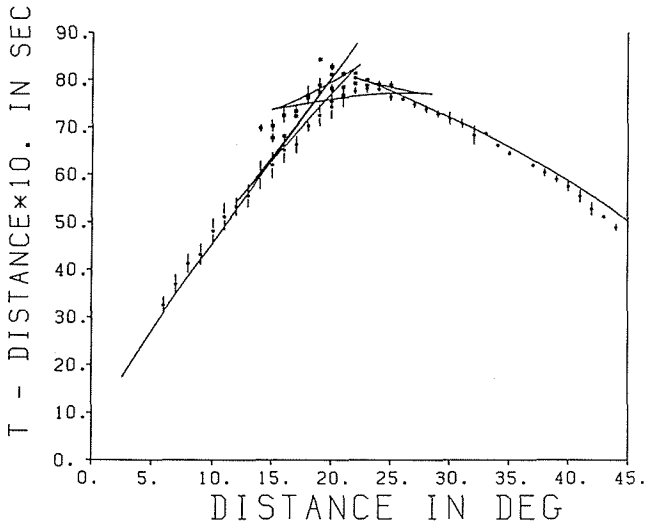

Figure 15: The comparion of the calculated travel time for model 14 with the observations.

5 Discussion

An important feature of model 12 is that it has the second discontinuity at a greater depth and with a larger velocity contrast than Fukao's (1977) model. We examine whether the difference in depth and velocity contrast between the two models is significant or not.

For that purpose we determine the best fitting model and its error bounds by assuming model 12 for the structure shallower than 644 km. Model 15 thus obtained is presented with its error bounds of the 95 % confidence level in Fig. 16. Both the depth and velocity contrast are nearly equal to those of model 12. This may indicate that the existence of the second discontinuity with a velocity contrast of 7 % around 700km is reasonable.

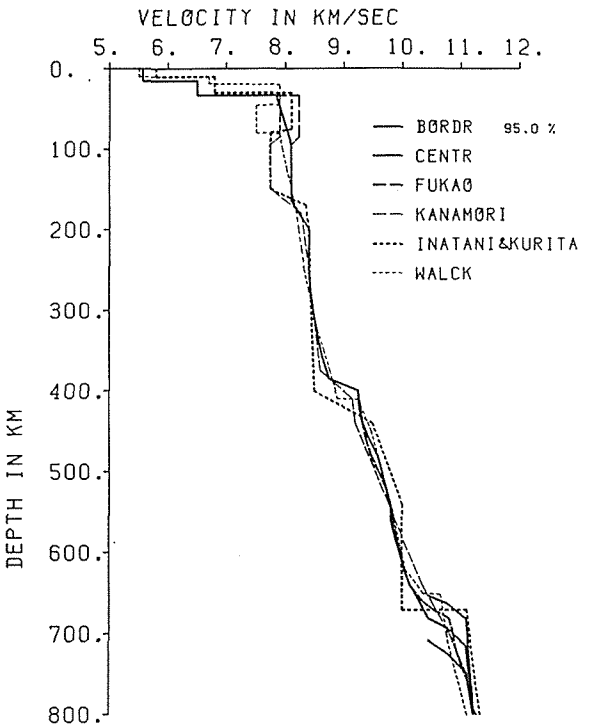

Figure 16: The velocity structure (model 15, designated as CENTR) with its bounds (designated as BORDR) obtained with the confidence level of 95.0 % by the $\tau - p$ inversion using the stripping depth of 644 km. The comparison is made with the models of Fukao (1977), Kanamori (1967), Inatani and Kurita (1980), and Walck (1985).

Figure 16 also shows the models of Kanamori (1967), Fukao (1977), Inatani and Kurita (1980), and Walck (1985) for comparison. The 660 km discontinuity of Fukao's model is within the bounds of 95 % confidence level.

Even if we lower the confidence level down to 50 %, it is still within the bounds. Therefore the difference of the 660 km discontinuity between our model and Fukao's model might be insignificant. Kanamori's model passes in the middle of the error bounds of our model. The velocity contrast of Inatani and Kurita's model is obviously larger than that of our model. The depth of the discontinuity is shallower in Walck's model than in our model. On one hand her model concerns the northeastern rim of the Pacific. On the other hand the other models represent the northwestern rim or the western marginal sea of the Pacific. We could probably say that the 660 km discontinuity is deeper in the northwestern rim of the Pacific than in the northeastern rim. Our recent study of the P-wave structure for the western Pacific rim using a different data set (Kato and Nakanishi, 2000) suggests the depth of 700 km for the 660 km discontinuity, and may support the result of the present study.

The result of the present study may suggest the depression of the 660 km discontinuity beneath the Kuril-Aluetian arc, where the old Pacific plate (65 - 135 Ma: Cretaceous) (Pitman et al., 1974) is subducted and the cold leading edge of the plate must cool the mantle surrounding the 660 km discontinuity beneath this region.

The high-pressure experiment made by Ito and Takahashi (1989) shows the negative value of dP/dT (P: pressure, T: temperature) of Clapeyron curve for the dissociation of spinel $(Mg,Fe)_2SiO_4$ (γ) to perovskite $(Mg,Fe)SiO_3$ (Pv) and magnesiowüstite $(Mg,Fe)O$ (Mw), which is considered to be the most plausible candidate for the 660 km discontinuity. They obtain dP/dT = -0.0028 GPa/K for the phase boundary of γ and $Pv + Mw$. If the temperature in the upper mantle at the depth of 660 km discontinuity is lower by 100°K in the subduction region than in the surrounding regions, the temperature difference increases the pressure of the phase change by 0.28GPa, which is equivalent to the depth increase of about 10 km. Thus a temperature decrease of about 300°K is required to explain the depth difference of 30 km.

Thermal structure of the subduction region has been modelled by many scientists but the temperature distributions from these studies are broadly similar to each othrer. Here we take the modelling result obtained by Shubert et al. (1975). In their model the temperature difference between the cold slab and the neighboring mantle is about 700°K near the 660 km discontinuity. However, the temperature decrease due to the cold slab is rather small in the oceanic mantle beneath the trench and it seems difficult to interpret the depth difference of 30 km in terms of only the thermal structure. Further discussions with consideration of convection, gravity, and mineral compositions are beyond the scope of the present paper.

The result of Kato and Nakanishi (2000) also supports that the 660km discontinuity is depressed beneath the subduction region. However, it is still difficult to rule out the possibility of the measurement errors. Analysis of broadband digital waveform data recorded by the seismological networks deployed for the last decade can reduce the measurement errors and can show up the undulations of the upper mantle discontinuities.

6 Conclusion

We obtained the upper mantle P-wave structure of the northwestern rim of the Pacific Ocean. Model 12, which can be considered the best model in the sense of the best explaining the observations, is characterized by: (1) It has no low velocity zone. (2) The velocity of the uppermost mantle gradually increases from 7.84 to 8.10 km/s in the depth range of 33-95 km and is constant in the depth range of 95-165 km and abruptly increases at depths 165-200 km. (3) The 410 km discontinuity is almost identical with that of Fukao's (1977) model (FK) which has an increase of about 6 % in velocity near 390 km. (4) There is a minor transition zone around 460 km, the depth of which is shallower than that of FK. The velocity contrast is 3 %. (5) The depth of the 660 km discontinuity is 700 km, which is greater than that of FK. The velocity increase is 0.70km/s or 7 %, which is a little larger than that of FK.

We obtained the velocity bounds that include all velocity-depth curves which agree with the observational $\tau(p)$ data within a statistical limit to know how large the uncertainties of data reflect in the modeling result. For the discontinuity at 700 km the error bounds obtained by the $\tau - p$ inversion include FK within the 95 % confidence interval. Therefore we cannot say that the character (5) of model 12 is significant. However, the comparison with other models obtained for the regions along the rim of the Pacific might imply that the 660 km discontinuity is locally deep beneath northwestern rim. We need more abundant data of secondary waves to make a definitive conclusion on the regional difference of the 660 km discontinuity.

Recently we have made a study of the upper mantle P-wave structure of the western Pacific rim using a different seismological network (Kato and Nakanishi, 2000) and the result (model sn12c, which is obtained by correcting the model 12 of the present study (Fig. 11 and Table 2)) may support the depth of 700 km obtained in the present study.

Using the aray analysis we showed that the waves from the events at distances less than 20° arrived at Hokkaido from the direction rotated clockwise from the expected direction to the ocean side of the Kuril arc. This means

that the assumption of the lateral velocity homogeneity is invalid. Therefore we may have to consider the three-dimensional velocity variation to obtain more accurate velocity structure beneath the region with a strong lateral velocity contrast. The northwestern rim of the Pacific Ocean, where the high velocity plate contacts with the low velocity marginal sea, is an example of such region.

Acknowledgments: We thank the Research Center for Earthquake Prediction of Hokkaido University for providing the seismograms used in this study. We thank Y. Motoya for computer programs for optical disk. The computations were made at the Hokkaido University Computing Center. The publication of the present paper is encouraged by the recent study with M. Kato, by N. Imasato, and by financial supports from Yamada and Kurata Science Foundations. T. Awaji gave us stylistic comments which improved the readability of the paper.

References

Adams, R. D., *Bull. Seismol. Soc. Am.*, **61** (1971), 1441-1451.

Aki, K. and P.G. Richards, *Quantitative Seismology*, H. W. Freeman and Company, San Francisco, Calif. (1980), 932pp.

Anderson, D.L. and M.N. Toksöz, *J. Geophys. Res.*, **68** (1963), 3483-3500.

Bessonova, E.N., V.M. Fishman, V.Z. Ryaboyi, G.A. Sitnikova, *Geophys. J. R. Astron. Soc.*, **36** (1974), 377-398.

Dziewonski, A.M. and F. Gilbert, *Geophys. J. R. Astron. Soc.*, **44** (1976), 7-17.

Engdahl, E. R. and E. A. Flinn, *Science*, **163** (1969), 177-179.

Fukao, Y., *Geophys. J. R. Astron. Soc.*, **50** (1977), 621-642.

Hamada, K., *J. Phys. Earth*, **21** (1973), 463-474.

Hamada, N., *Pap. Meteorol. Geophys.*, **35** (1984), 109-167 (in Japanese with English abstract).

Ichikawa, M. and E. Mochizuki, *Pap. Meteorol. Geophys*, **22** (1971), 229-290 (in Japanese with English abstract).

Inatani, H. and K. Kurita, *Zisin, Ser. 2*, **33** (1980), 37-49 (in Japanese with English abstract).

Ito, E. and E. Takahashi, *J. Geophys. Res.*, **94** (1989), 10637-10646.

Jeffreys, H. and K.E. Bullen, *Seismological Tables*, British Assoc. Adv. Sci. Gray Milne Trust, London (1940), 50pp.

Johnson, L.R., *J. Geophys. Res.*, **72** (1967), 6309-6325.

Kanamori, H., *Bull. Earthq. Res. Inst. Tokyo Univ.*, **45** (1967), 657-678.

Kato, M. and I. Nakanishi, *Earth Planets Space*, **52** (2000), 459-466.

Katsura, T. and E. Ito, *J. Geophys. Res.*, **94** (1989), 15663-15670.

Kawasaki, I., S. Karato and T. Ouchi, *Zisin, Ser. 2*, **42** (1989), 239-254 (in Japanese with English abstract).

Kosarev, G., R. Kind, S. V. Sobolev, X. Yuan, W. Hanka, and S. Oreshin, *Science*, **283** (1999), 1306-1309.

Lawson, C.L. and R.J. Hanson, *Solving Least Squares Problems*, Prentice-Hall, Englewood Cliffs, N.J. (1974), 340pp.

Nakanishi, I., *Geophys. Res. Lett.*, **13** (1986), 1458-1461.

Nakanishi, I., *Geophys. J.*, **93** (1988), 335-346.

Nakanishi, I., *J. Phys. Earth*, **37** (1989), 297-301.

Nakanishi, I. and Y. Motoya, *J. Phys. Earth*, **38** (1990), 163-177.

Niazi, M. and D.L. Anderson, *J. Geophys. Res.*, **70** (1965), 4633-4640.

Pitman, W. C., III, R. L. Larson, and E. M. Herron, *Isochron Map and Age Map of Ocean Basins*, Geol. Soc. Am., Boulder (1974).

Shearer, P. M., *J. Geophys. Res.*, **96** (1991), 18147-18182.

Shearer, P. M., *Geophys. J. Int.*, **115** (1993), 878-904.

Shearer, P. M., *J. Geophys. Res.*, **101** (1996), 3053-3066.

Shubert, G., D. A. Yuen, and D. L. Turcotte, *Geophys. J. R. Astron. Soc.*, **42** (1975), 705-735.

Stark, P.B., R.L. Parker, G. Masters, and J.A. Orcutt, *J. Geophys. Res.*, **91** (1986), 13892-13902.

Stark, P.B. and R.L. Parker, *J. Geophys. Res.*, **92** (1987), 2713-2719.

Utsu, T., *Geophys. Bull. Hokkaido Univ.*, **25** (1971), 99-128 (in Japanese with English abstract).

Vinnik, L. P., *Phys. Earth Planet. Inter.*, **15** (1977), 39-45.

Walck, M.C., *Geophys. J. R. Astron. Soc.*, **76** (1984), 697-723.

Walck, M.C., *Geophys. J. R. Astron. Soc.*, **81** (1985), 243-276.

Walck, M.C. and J.B. Minster, *J. Geophys. Res.*, **87** (1982), 1757-1772.